Title
An Autonomous Monolithic Wearable System for Diurnal Sweat Biomarker Data Acquisition and Analysis

Author
Hojaiji, Hannaneh

Publication Date
2020

Peer reviewed|Thesis/dissertation

UNIVERSITY OF CALIFORNIA

Los Angeles

An Autonomous Monolithic Wearable System for Diurnal Sweat Biomarker Data Acquisition and Analysis

A thesis submitted in partial satisfaction

of requirements for the degree Master of Science

in Electrical and Computer Engineering

by

Hannaneh Hojaiji

2020

ABSTRACT OF THE THESIS

An Autonomous Monolithic Wearable System for Diurnal Sweat Biomarker Data Acquisition and Analysis

by

Hannaneh Hojaiji

Master of Science in Electrical and Computer Engineering

University of California, Los Angeles, 2020

Professor Sam Emaminejad, Co-Chair

Professor Asad M. Madni, Co-Chair

To track dynamically varying and physiologically relevant biomarker profiles in sweat, autonomous wearable platforms are required to periodically sample and analyze sweat with minimal user intervention. Previously reported sweat sensors are functionally limited to capturing biomarker information at one time-point/period, thereby necessitating repeated user intervention to increase the temporal granularity of biomarker data. Accordingly, we present a multi-compartment wearable system, where each compartment can be activated to autonomously induce/modulate sweat secretion (iontophoretically) and analyze sweat at set timepoints. This system was developed following a hybrid-flex design— vertically integrating the required functional modules: miniaturized iontophoresis interfaces, adhesive thin film microfluidic-sensing module, and control/readout electronics. The system was deployed in a human subject study to track the diurnal variation of sweat glucose levels in relation to the daily food intake. The

demonstrated autonomous operation for diurnal sweat biomarker data acquisition illustrates the system’s suitability for large-scale and longitudinal personal health monitoring applications.

The thesis of Hannaneh Hojaiji is approved.

William J. Kaiser

Peyman Benharash

Sam Emaminejad, Committee Co-Chair

Asad M. Madni, Committee Co-Chair

University of California, Los Angeles

2020

TABLE OF CONTENTS

LIST OF FIGURES

ACKNOWLEDGEMENTS

First, I would like to express my sincere gratitude to my advisors, Professor Sam Emaminejad and Professor Asad M. Madni, for their influential, professional, and valuable guidance and support throughout this work.

I would like to appreciate Professor William J. Kaiser and Doctor Peyman Benharash for serving as my thesis committee members and giving me dedicated, insightful, and valuable comments and advice, which have greatly helped me improve my work. It is my great honor to have them as my mentors and thesis committee members.

I would also like to thank Peter Staudhammer Northrop Grumman Fellowship donors for their support.

Additionally, I am grateful to work closely with great colleagues and students at Henry Samueli School of Engineering and Interconnected & Integrated Bioelectronics Lab. I am also thankful to my amazing friends in EGSA, HKN, TBP, and UCLA for their support and the wonderful memories we have made together.

Last but certainly not least, I would like to thank my dear and lovely family for their unconditional love, dedicated support, and sacrifices throughout this journey. Thank you for hearing me out, brainstorming on my ideas, cheering up for my successes, and teaching me the true meaning of family with your resilience and care through all the ups and downs.

I would like to acknowledge that my thesis is reproduced from some of my recent publications including Ref. Lab Chip, 2020,20, 4582-4591 and Ref. JMEMS, 2020,29(5), 1106-1108 with permission from the Royal Society of Chemistry (Lab On a Chip) and IEEE (© 2020 IEEE).

Chapter 1 Introduction

1.1 Background of wearable biosensing system

Wearable biomarker sensing platforms are poised to catalyze the transition from point-of-lab and point-of-care to point-of-person health and wellness monitoring as they provide frequent, real-time, and contextually relevant measures of informative biomarker molecules. Among the potential wearable solutions, sweat-based sensing modality particularly allows for accessing biomarker molecules non-invasively. Accordingly, various sweat bioanalytical platforms were developed (typically implemented as a disposable biochemical sensor unit interfacing a control/readout circuit module) and utilized to target biomarker molecules such as metabolites, electrolytes, and nutrients [1-5]. However, the presented platforms are functionally limited to one time-point/period biomarker data recording. To acquire biomarker information at multiple points during the day, frequent thermal/exercise-based or iontophoresis-based (manually set up) sessions are required to access sweat, and pristine microfluidic/sensor unit replacements are necessary to avoid sample/sensor contamination. Therefore, the underlying limitations of such wearable sweat platforms prohibit their translation into large-scale and longitudinal personal health monitoring applications [1-12].

1.2 Integration and clinical utility

Here, to address such limitations, we devise a multi-compartment wearable system, where each compartment can be programmatically activated to induce/modulate sweat secretion (*via* iontophoretic actuation) and analyze sweat at intermittent time-points. This system was realized within a compact footprint, following an introduced hybrid-flex system design and seamless integration methodology—integrating the required functional modules: 1) an array of iontophoretic actuation interfaces, where each interface can be independently programmed to

activate/modulate sweat secretion; 2) a laser-patterned thin tape-based microfluidic module for sweat sampling and routing; 3) electrochemical sensing interfaces, which are functionalized on an anisotropic conductive adhesive (ACA) substrate to facilitate seamless biomarker signal transduction to the electronics within the microfluidic module; and 4) a kirigami-inspired and multi-layered flexible printed circuit board (FPCB) to execute system-level functionalities, including tunable iontophoresis (to modulate secretory agonist delivery and thus sweat secretion), sensor signal acquisition/processing, and biomarker data display/wireless transmission.

As a self-sufficient solution, the integrated hybrid-flex wearable system realizes core functionalities such as sweat stimulation at the desired time and secretion rate, *in-situ* signal processing, real-time data display, and bidirectional data communication with phone/cloud server. By automating these operations, delivered within the devised multi-compartment configuration, we enabled the tracking of the diurnal profile of glucose, as an illustrative biomarker with clinical significance.

1.3 Operational principle of the hybrid-flex system

The skin adherable hybrid-flex system (Fig. 1.1a) is realized following a vertical integration scheme, integrating various functional modules: miniaturized iontophoresis interfaces, adhesive thin film microfluidic-sensing module, and control/readout electronics (Fig. 1.1b).

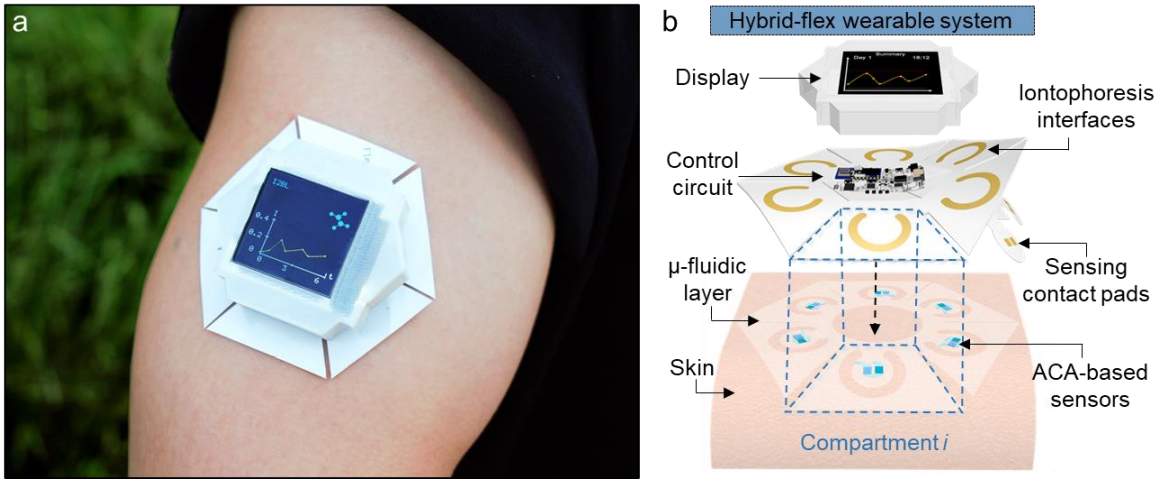

Figure 1.1: a) Image of the developed hybrid-flex wearable system adhered to a subject's arm. b) Exploded schematic of the multi-compartment system, demonstrating vertical integration of an FPCB with iontophoresis electrode arrays (radially fabricated on the backside of the FPCB) and a microfluidic-sensing module.

The system is implemented as a kirigami-inspired multi-compartment configuration, where linear incisions—in hexagonal-shaped FPCB and microfluidic-sensing modules—were utilized to render flap-like compartments, thus providing the mechanical degree of freedom necessary for structural compliance with skin. In this configuration, each compartment can be individually addressed to induce/modulate sweat secretion (via iontophoretic actuation) and analyze sweat at set time-points (Fig. 1.2a).

The iontophoretic sweat induction is achieved with the aid of a digitally programmable current source and a miniaturized iontophoresis electrode/hydrogel array. This implementation allows for the tunable delivery of secretory agonist molecules (embedded in hydrogel) underneath the skin, simply by adjusting the iontophoresis current level/duration, thus enabling the modulation of the sweat secretion profile. In our design, the iontophoresis electrodes are monolithically integrated

within the FPCB module: the positive semi-annular electrodes fabricated on the backside of the FPCB flaps, radially arranged around a shared circular negative electrode (on the backside of the center of FPCB). Furthermore as shown in Fig. 1.2a, the semi-annular design of the positive iontophoresis electrodes facilitates a lateral pathway [5] for the stimulation of neighboring sweat glands (that are vertically below sweat sampling microfluidic interface, but laterally away from the iontophoresis interface).

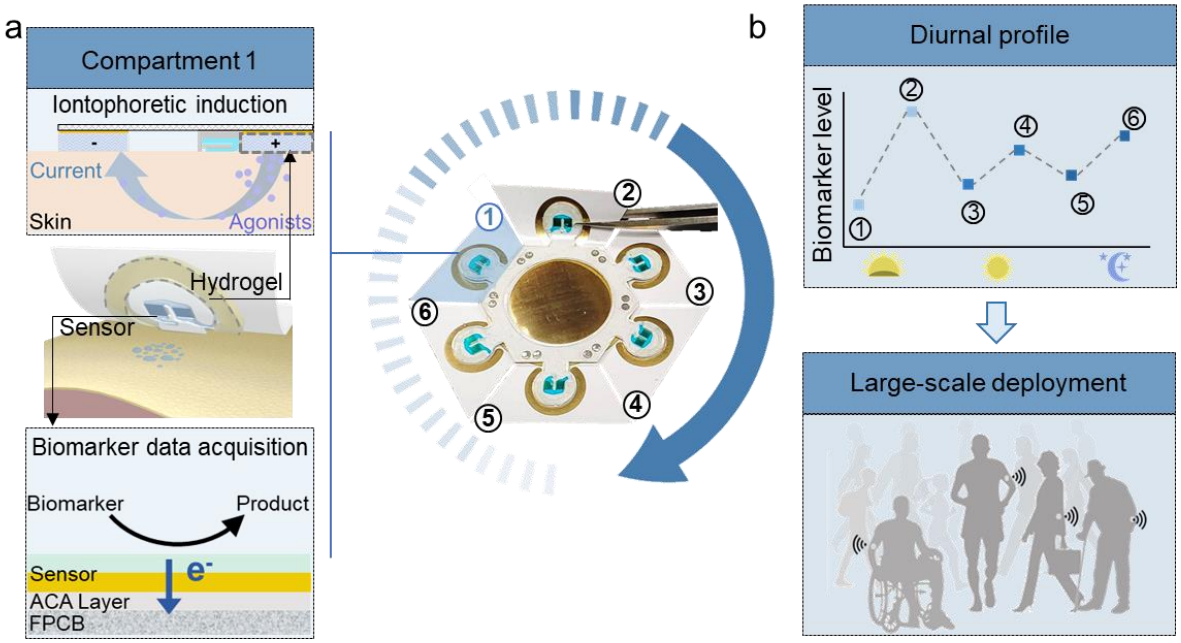

Figure 1.2: a) Schematic representation of bioanalytical operations (left: iontophoresis, sensing) delivered by each of the compartments (right: bottom view photograph of the developed hybrid-flex wearable system) that can be programmatically activated at intermittent time points to obtain biomarker data. b) Conceptual illustration of positioning the autonomous system to track the diurnal biomarker profiles for population-level health monitoring.

The collection and analysis of secreted sweat is achieved with the aid of a thin-film microfluidic-sensing module, featuring an array of microfluidic sensing chambers, (Fig. 1.3) where each sensing

chamber is paired with an iontophoresis interface. The sensing interfaces are engineered on an ACA film. In this way, the adhesive and vertical conductivity of the film can be exploited to interconnect the transduced signal to the readout circuitry of the FPCB, in-situ, via monolithically integrated sensing contact pads. By programming the FPCB, the compartments within our system can be activated at set time points during the day to render biomarker readings autonomously and non-invasively. Therefore, as conceptualized in Fig. 1.3b, the devised solution presents great potential to facilitate longitudinal monitoring of biomarkers across the general population.

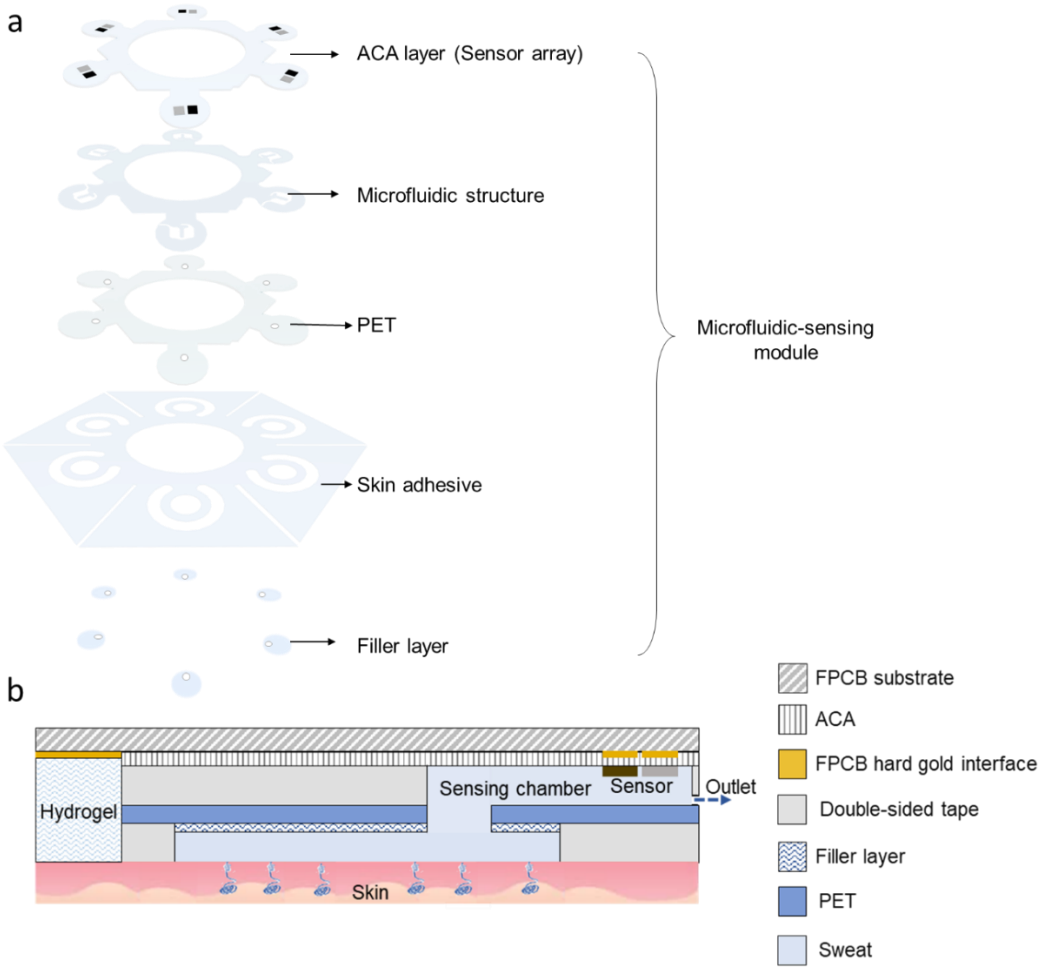

Figure 1.3: a) Exploded view of the microfluidic-sensing module. b) Cross-section view of the microfluidic-sensing module-skin interface.

Chapter 2 Iontophoresis: design and system-level integration

2.1 Iontophoresis process

As an active sweat induction method with high epidermal analyte flux, iontophoresis uses an electrical current to deliver secretory agonist molecules to stimulate the sweat glands. In this way, by adjusting the applied electrical current, the agonist dosage and timing of the sweat secretion can be accurately controlled. However, the commercially available iontophoretic sweat induction (*e.g.*, Macroduct and Nanoduct) and sampling tools are bulky, require large agonist-loaded hydrogel-skin area interfaces (~5 cm^2/per electrode), and rely on multi-step and manual operations, inherently preventing their large-scale deployment for longitudinal studies. To realize a scalable sweat sampling tool suitable for large scale studies, we devised an autonomous sweat sampling patch, the core of which is an addressable array of miniaturized and coupled iontophoresis/microfluidic interfaces. In this implementation, each element of an array can be activated on-demand or at scheduled time-points to induce/collect sufficient sweat samples for analysis. To achieve effective and safe sweat induction within a compact footprint, here, we particularly introduced a design space, to satisfy interdependent constraints imposed by sufficient agonist delivery and maintaining minimal skin temperature rise.

2.2 Design of iontophoresis interface

Commercial iontophoresis interfaces (*e.g.*, Macroduct and Nanoduct) rely on using relatively large electrodes [13] for sweat induction and sampling from the stimulated skin area, both of which are incompatible for the envisioned wearable applications. To miniaturize the iontophoresis interface, we need to consider the interdependent constraints: sufficient agonist delivery (proportional to the level and duration of the applied current) and maintaining the subsequently increased skin temperature (proportional to the duration of application and square of current density) within a

safe operational range.

The amount of the agonist delivered (P, in mg), to the first order, can be estimated by the following equation:

$$P = \frac{I\ t\ M}{F} \tag{1}$$

where I is in iontophoresis current in mA, t is the duration of iontophoresis application in seconds, M is the molecular weight of the agonist, and F is the Faraday constant (96489 C/mol).

Following (1), and assuming pilocarpine as the agonist (systemic dosage: 10 mg [14], effectively setting an upper-bound) with 50% delivery efficiency [14], we calculated and plotted, in Fig. 2.1a, the amount of the delivered agonist molecules. Additionally, we estimated the increase in skin temperature (ΔT, Fig. 2.1b) by assuming that the electrical energy is dissipated as heat following the joule heating phenomenon, where $\Delta T \propto J^2\ t\ R$ (J: current density, R: skin resistivity) [15]. It is worth noting that the presence of hydrogel lowers the electrical resistance of the stratum corneum, which is particularly useful in reducing the ΔT [15], [16]. Based on these estimations, Macroduct (I = 1.5 mA, t = 5 min) and Nanoduct (I = 0.5 mA, t = 2 min) [13] interfaces deliver agonists on the order of 0.1-1 mg while the estimated skin temperature increase does not exceed the safety threshold (~6 °C [15]). As annotated in Fig. 2.1, for our iontophoresis interface, we selected operational parameters (I = 0.6 mA, t = 5 min) and electrode size (0.6 cm^2), as an allowable operational point within the identified space, which ensures sufficient agonist delivery (~0.5 mg) with minimal temperature increase. Furthermore, to facilitate a lateral pathway for the stimulation of target sweat glands (that are vertically below the microfluidic interface, but laterally away from the induction interface), we used a ring-shaped iontophoresis configuration.

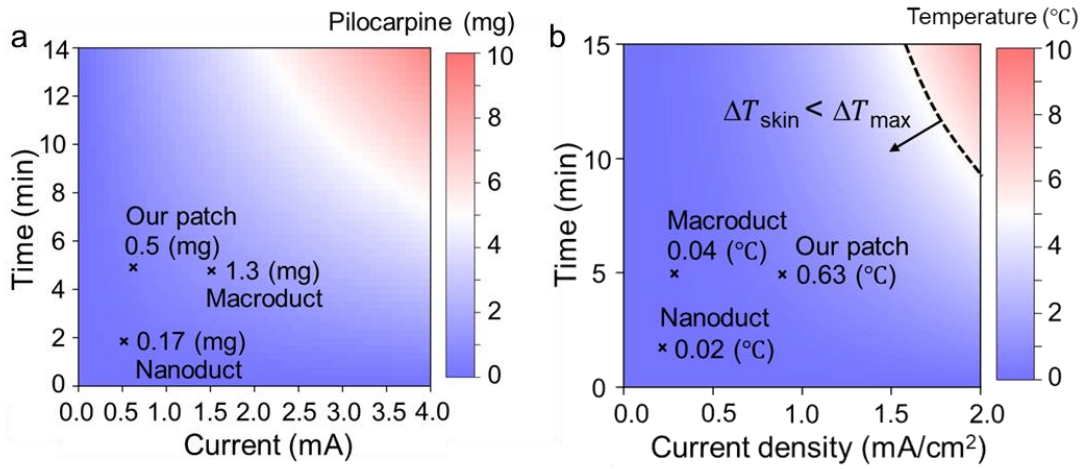

Figure 2.1: a) Estimated amount of the delivered pilocarpine for different iontophoresis current levels and durations. b) Estimated increase in the skin temperature for different iontophoresis current density levels and durations. The dashed line indicates the conditions leading to maximum allowable temperature rise for the skin. The calculated dosages and skin temperature increments for our patch and two commercially available devices are annotated (© 2020 IEEE).

The programmable iontophoresis characterization and diurnal human subject studies were performed with our wearable system. The commercial agonist-loaded hydrogel discs (0.5% pilocarpine nitrate, [17], PILOGEL®, Wescor Inc., South Logan, Utah) were reshaped (using custom-designed 3D printed molds) to fit the semi-annular positive iontophoresis electrode array. The programmable iontophoretic stimulation was then performed following the sweat stimulation settings described in the following section.

2.3 Miniaturized iontophoresis interface for sweat secretion modulation

First, the robustness of the iontophoresis current delivery under mechanical deformation was tested under three iontophoresis electrode bending conditions (flat; α = 60°, R = 15 mm; and α = 30°, R = 10 mm, Fig. 2.2a), where the applied iontophoretic current was continuously monitored. The results demonstrate that the effect of bending on iontophoresis current was negligible (Fig. 2.2b).

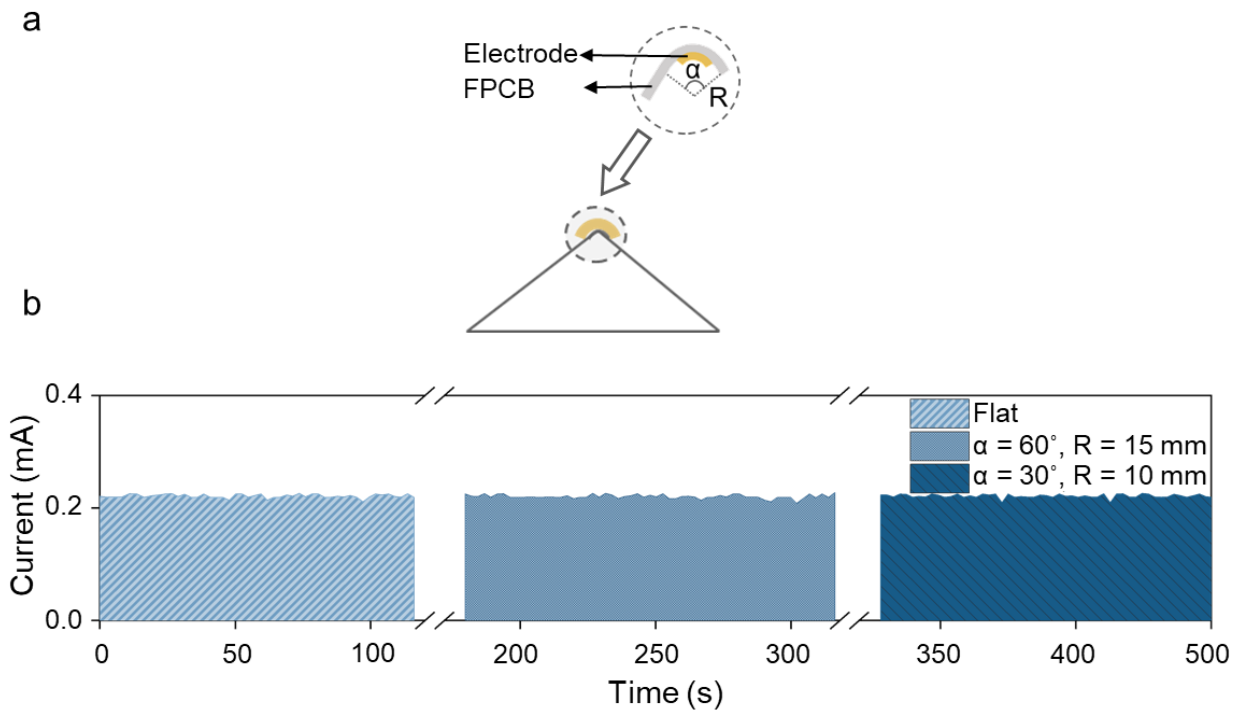

Figure 2.2: a) Illustration of the setup for iontophoresis current characterization, performed under three bending conditions (1. no bending, 2. α = 60°, R = 15 mm, and 3. α = 30°, R = 10 mm). b) Real-time iontophoresis current recordings under corresponding bending conditions (programmed current: 0.2 mA, CV for all cases < 1.5%).

Then, the consistency of the iontophoretic operations across all six compartments and for different physiologically relevant skin conditions (~300 Ω to ~100 kΩ [18]) was evaluated, *ex situ*, by monitoring the applied current through representative skin impedance loads. As shown in Fig. 2.3, the iontophoresis current differences across all six compartments were less than 0.9% (R_{skin} = 47 kΩ). Similarly, the variation in the load impedances had minimal effect on the delivered current level (Fig. 2.3 inset).

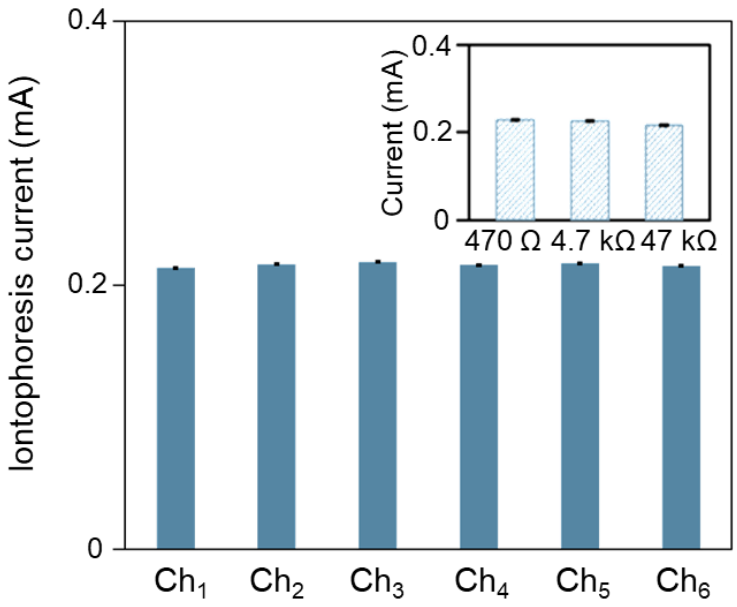

Figure 2.3: Demonstration of consistent iontophoresis current delivery across all compartments (load: 47 kΩ, programmed current: 0.2 mA, Δ = 0.9%). Inset shows load-independent iontophoresis current delivery capability of the system. Error bars indicate standard error (n = 6 compartments). Δ is calculated as a percent variation of the maximum measured current level from the baseline average value.

To evaluate the stability of on-body iontophoresis stimulation by our wearable system, we performed iontophoresis in the presence of body motions with different intensities. Figure 2.4 illustrates a stable iontophoresis current profile (negligible current fluctuation, coefficient of variation (CV) < 2%) was delivered under varying body motion frequencies and accelerations (from ~0 to ~20 Hz, and from ~0 to ~20 m/s^2 respectively).

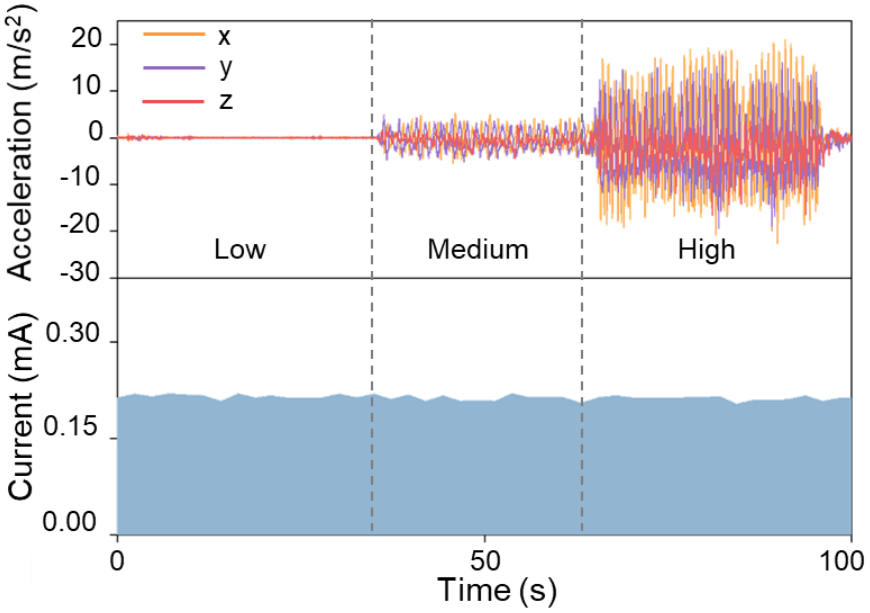

Figure 2.4: *In-situ* characterization of iontophoresis current stability on the body under different exercise intensities (programmed current: 0.2 mA).

2.4 Sweat secretion rate characterization using standard lab instruments

The capability to program sweat secretion rate was first examined (Fig. 2.5) using standard lab instruments. Pilocarpine hydrogels (1% pilocarpine nitrate) were fabricated, following the previously introduced method [19]. These hydrogels were molded into donut-shaped gels (area: 3.2 cm^2), and were used to iontophoretically stimulate sweat on the volar surface of the two

forearms (alternating between the two arms at each point) for the two subjects using a commercial Q-sweat system (WR Medical Electronics Co. Maplewood, MN). By varying the applied current and duration of iontophoresis, the iontophoretic dosage was tuned for each stimulation datapoint. The commercial sweat-rate sensor (Q-sweat, WR Medical Electronics Co.) was mounted onto the skin, at the center (area: 0.8 cm^2) of the donut-shaped positive electrode, to measure sweat secretion rate for the corresponding iontophoretic dosage. The sweat secretion rate was continuously measured for 10 minutes from the time of the stimulation started and data points represent the plateau of the sweat rate.

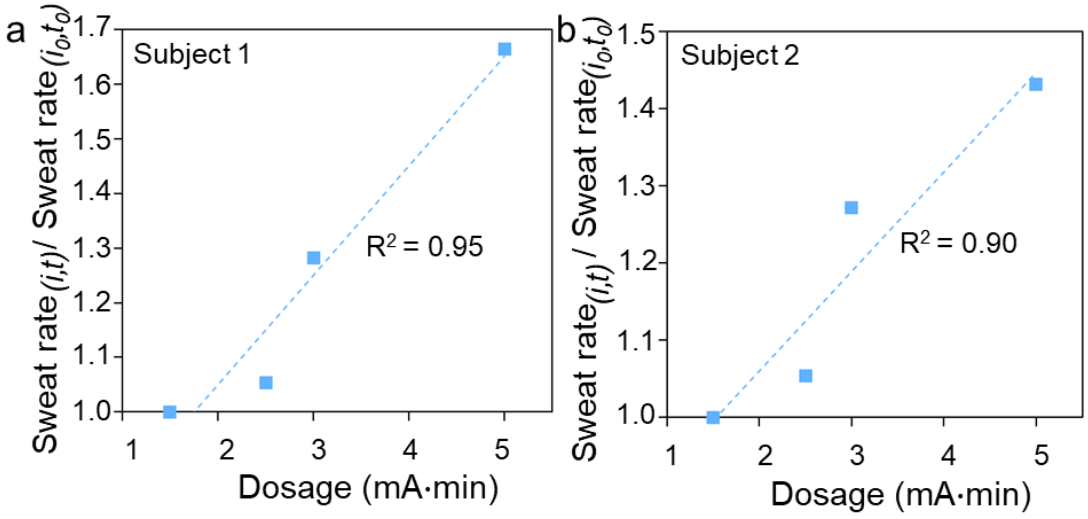

Figure 2.5: Sweat secretion rate *vs.* iontophoretic dosage for subject 1 (a) and 2 (b). The normalized sweat rate is obtained by dividing the measured sweat rate with the iontophoretic dosage ($I_n \times t_n$) by the sweat rate with the dosage ($I_0 \times t_0$) = (0.5 mA × 3 min).

2.5 Characterization of the programmable iontophoresis

By capitalizing on the capability of our system in tuning the iontophoresis current level and duration of the stimulation, we can control the amount of agonists delivered to the glands, thus allowing us to effectively program the secretion profile and adjust the secretion rate/volume. To examine our ability to program the secretion rate, first, we performed sweat stimulation (utilizing standard lab instruments) on two subjects, where in each of the cases we varied I and t (I = 0.5, 1 mA; t = 3, 5 min). As shown in Fig. 2.5, our sweat secretion characterization results (performed with an evaporimeter) illustrated that higher $I \times t$ conditions (iontophoretic stimulation dosage) led to higher secretion rates for both subjects. We can also exploit our programmable sweat induction capability to ensure harvesting sufficient sweat sample volumes for reliable *in-situ* analysis. To illustrate this point, using our solution, we performed sweat stimulation (two trials) with different iontophoresis current levels and fixed duration (on nearby spots of the volar surface of the subject's arm) and secretion characterization with a spiral-shaped microfluidic sweat collector (Fig. 2.6).

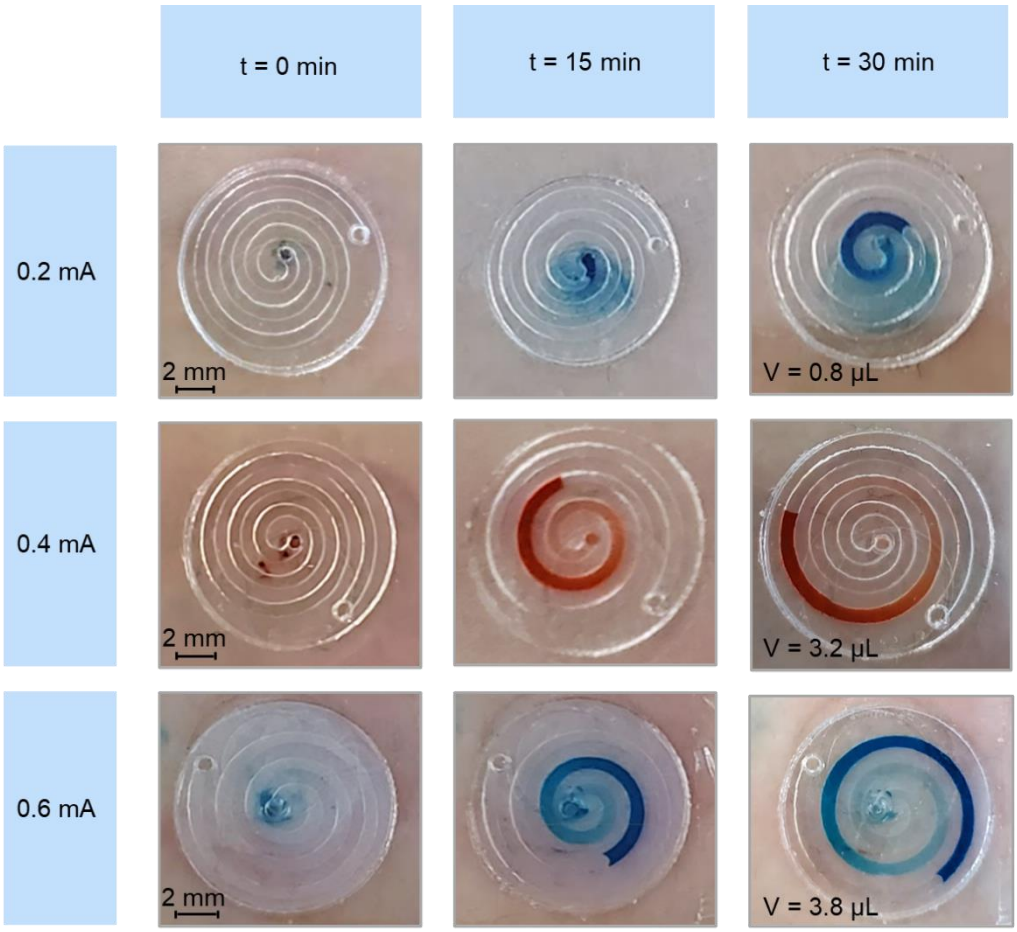

Figure 2.6: Optical sweat secretion characterization (with the aid of color dyes embedded in the channel), following three different iontophoresis current levels.

As shown in Fig. 2.7, for both trials, the increased iontophoresis current led to larger secreted sweat sample volumes. Furthermore, we can exploit our programmable sweat induction capability to elicit sweat secretion at desired time-points during the day, which is instrumental in the envisioned diurnal biomarker monitoring application. To illustrate this point, we deployed our multi-compartment system in a human subject study, where we programmed the compartments to be activated at different time points to induce sweat. As illustrated in Fig. 2.8, sufficient sweat sample volume (> 2 µL) was consistently induced across the six compartments during a day.

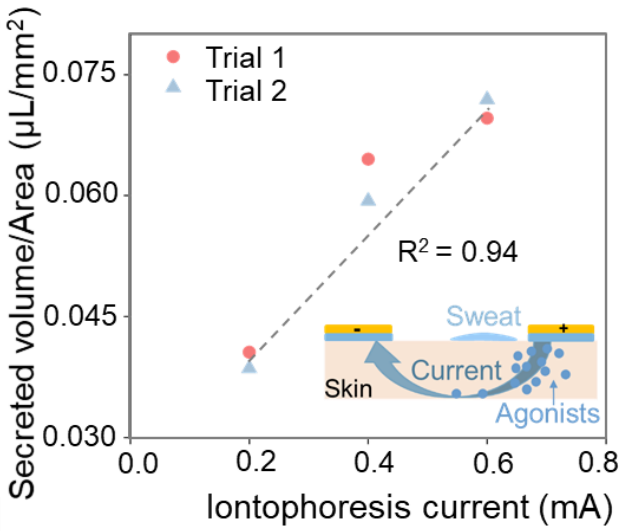

Figure 2.7: Tunable sweat secretion rate achieved by programming the iontophoresis current (rendered by our wearable platform, area of stimulation: 0.64 cm^2, corresponding to a current density of ~ 0.3 mA/cm^2 for I_0 = 0.2 mA). Inset shows the iontophoretic sweat agonist delivery process.

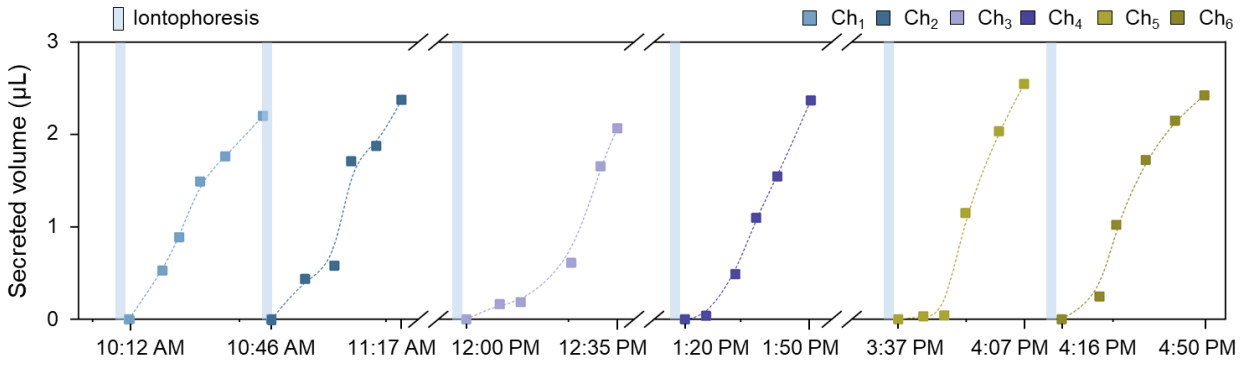

Figure 2.8: Intermittent sweat induction throughout a day using six sequentially activated compartments (I = 0.6 mA, t = 5 min).

We further verified that the accumulation of sweat due to natural perspiration over an extended amount of time (> 7 hours) and upon a moderate elevation in ambient temperature (6 °C) is negligible (Fig. 2.9). To avoid contamination of sensors due to sweat induction by non-iontophoretic mechanisms (*e.g.*, physical exercise), electronically-programmable microfluidic valves [20, 21] can be incorporated at the entry points of the sensing chambers.

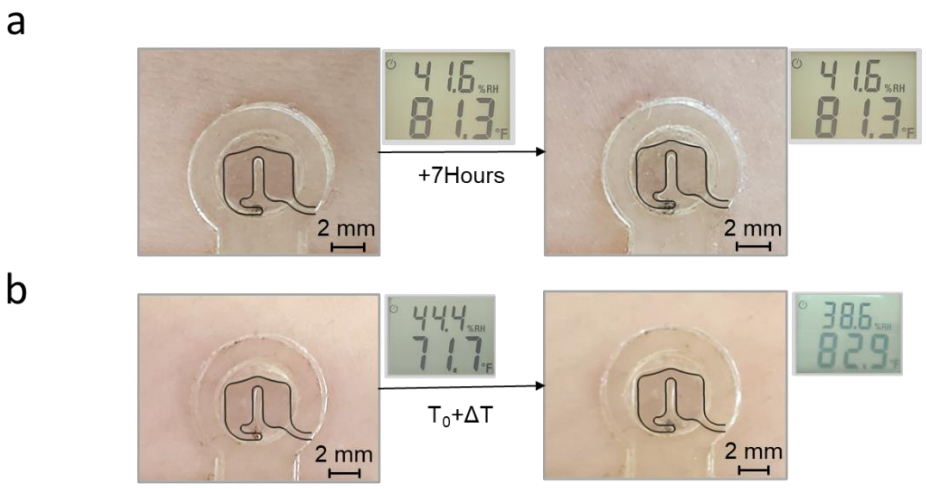

Figure 2.9: a) Optical image of a compartment illustrating negligible accumulation of sweat sample due to natural perspiration after 7 hours of non-labor daily activities. b) Optical image of a compartment illustrating negligible accumulation of sweat sample (over 2 hours) upon a moderate increase in the ambient temperature from ~ 22 °C to ~ 28 °C (equivalently, ~ 72 °F to ~ 83 °F, as measured and shown by a lab digital thermometer).

Chapter 3 3D microfluidic architecture for biofluid sampling and sensing

3.1 Tape-based microfluidic module fabrication scheme

To enable efficient routing and housing of µL-volumes of sweat, a thin-film microfluidic module is fabricated, following a rapid, and low-cost fabrication scheme. As shown in Fig. 3.1, the thin film microfluidic-sensing module is fabricated following a cost-effective and scalable microfluidic fabrication scheme [22] based on laser patterning and stacking double-sided tape and polyethylene terephthalate layers. The adhesive coating of the epidermal-facing layer and the thinness of the complete flexible module altogether render a stable device-epidermal contact as well as efficient and microliter-level sweat sampling.

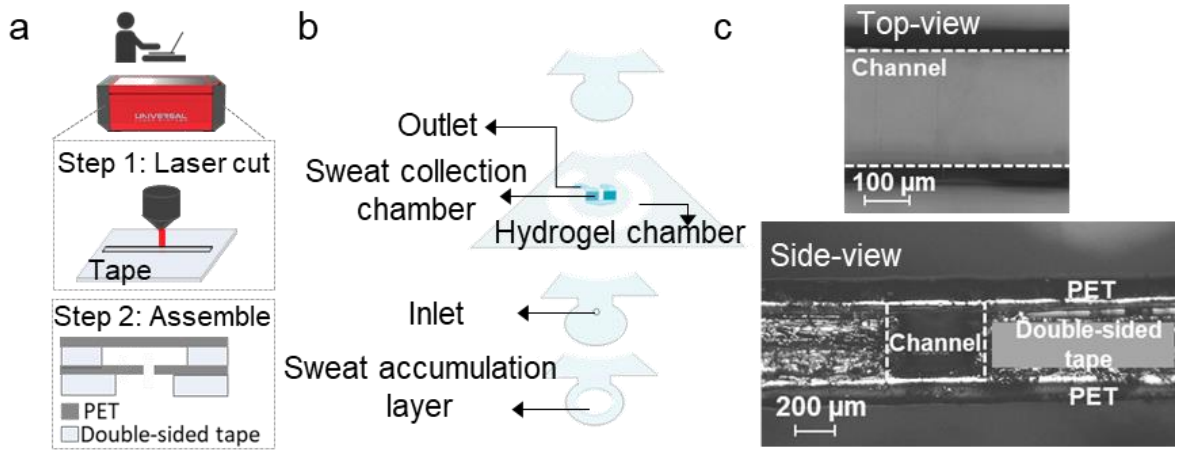

Figure 3.1: a) Fabrication procedure of the tape-based thin-film microfluidic module. b) Exploded view of the microfluidic module. c) Optical microscope images of the side and top views of the tape-based microfluidic channel (two layers of PET sandwiching dual-layered laser-cut double-sided tape) (© 2020 IEEE).

3.2 Fabrication and assembly of the microfluidic-sensing module

The thin film microfluidic-sensing module consists of an ACA-based sensing layer, a microfluidic structure layer (170 μm-thick, 9474LE double-sided tape, 3M), polyethylene terephthalate (PET, MG Chemicals, ~100 μm), a skin adhesive layer (170 μm-thick, 9474LE double-sided tape, 3M), and a filler layer (Scotch single-sided self-seal laminating sheets, 3M, USA). We use a laser-cutter (VLS2.30, Universal Laser Systems) to form 2D patterns of microfluidic channels/chambers in the microfluidic structure and skin adhesive layers, and biofluid inlets (d = 0.5 mm) in the PET and filler layers. The microfluidic-sensing module was assembled by vertically stacking these layers. On one side, the module adheres to the FPCB through the ACA layer, and on the other side, adheres onto the skin through the skin-adhesive layer. Additionally, the skin-adhesive layer (the flap-like patterns) also supports the hydrogel (within a 3D printed encapsulated mold) array interfacing with the skin.

Chapter 4 ACA-based electrochemical sensor development

4.1 Electrochemical sensor design

The electrochemical sensors are fabricated on an ACA substrate, following a mediator-free enzymatic sensor development protocol. Our electrochemical sensing interface consists of an enzyme layer (glucose oxidase), a PPD layer, and a PtNP/Au layer (Fig. 4.1). The PPD layer serves as a permselective membrane to reject interfering species in the sweat matrix [23, 24], and the PtNP/Au layer facilitates the oxidation of the end-product (here, H2O2) generated from enzyme-catalyzed reaction.

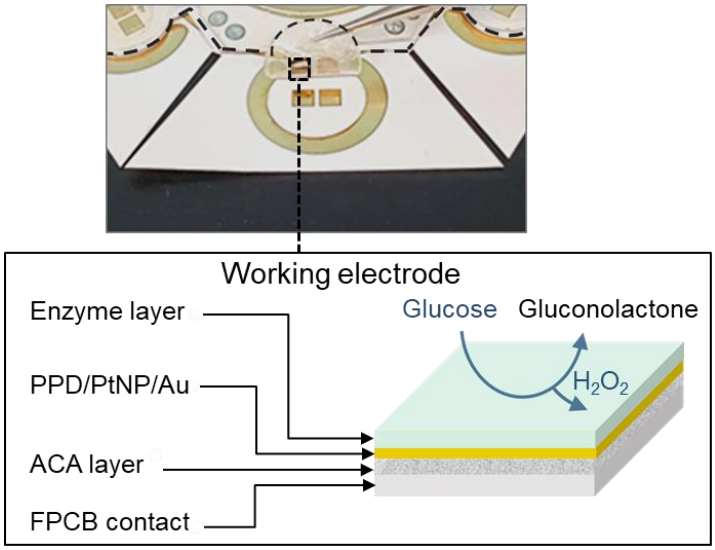

Figure 4.1: Integration of the disposable microfluidic-sensing module onto the corresponding FPCB contact pad and illustration of the sensing layers/mechanism for the developed glucose sensor.

Similar sensor development protocols can be adopted to construct sensing interfaces targeting other biomarkers by incorporating suitable biorecognition and functional layers: for example, an

ACA-based lactate sensing interface can be created (Fig. 4.2) by utilizing lactate oxidase as a biorecognition layer, coupled with PVC as a functional layer (diffusion limiting).

To fabricate thin-film electrochemical sensors, first, gold (Au) was deposited and patterned on an ACA substrate (9703, 3M, 50 μm). Then, platinum nanoparticles (PtNP) were electro-deposited onto the ACA/Au [25]. The biosensing interface was constructed by electrochemically depositing poly-*m*-phenylenediamine (PPD) layer onto the PtNP/Au/ACA by applying + 0.85 V (*vs*. Ag/AgCl) for 300 s in a fresh phosphate-buffered saline solution (Gibco® PBS, ThermoFisher, pH 7.2) with 5 mM *m*-phenylenediamine (Sigma-Aldrich). A 1% chitosan solution was thoroughly mixed with a glucose oxidase solution (Sigma-Aldrich, 50 mg/mL in PBS, pH 7.2) at a ratio of 1:1 (volume/volume). The glucose sensing interface was realized by drop-casting 1 μL of the aforementioned mixture onto the PPD/PtNP/Au/ACA electrode (4 mm^2) [26]. To create the lactate sensor, a 4 μL lactate oxidase solution (Toyobo, 50 mg/mL in PBS) was deposited onto PtNP/Au/ACA electrode and dried at room temperature, followed by drop-casting of a 2 μL 1% Chitosan solution and a 2 μL 3% polyvinyl chloride (PVC, Sigma-Aldrich) solution. To characterize the developed electrochemical sensor, constant potential amperometric measurements were conducted at + 0.3 V *vs*. Ag/AgCl. The amperometric response was recorded by a potentiostat (CHI 660E) or the custom-developed PCB. By drop-casting different concentrations of the target analytes onto the sensors' surface, a series of calibration curves were obtained. The sensor selectivity tests were performed in PBS buffer (pH 7.2) by the stepwise addition of different interfering species and glucose into PBS.

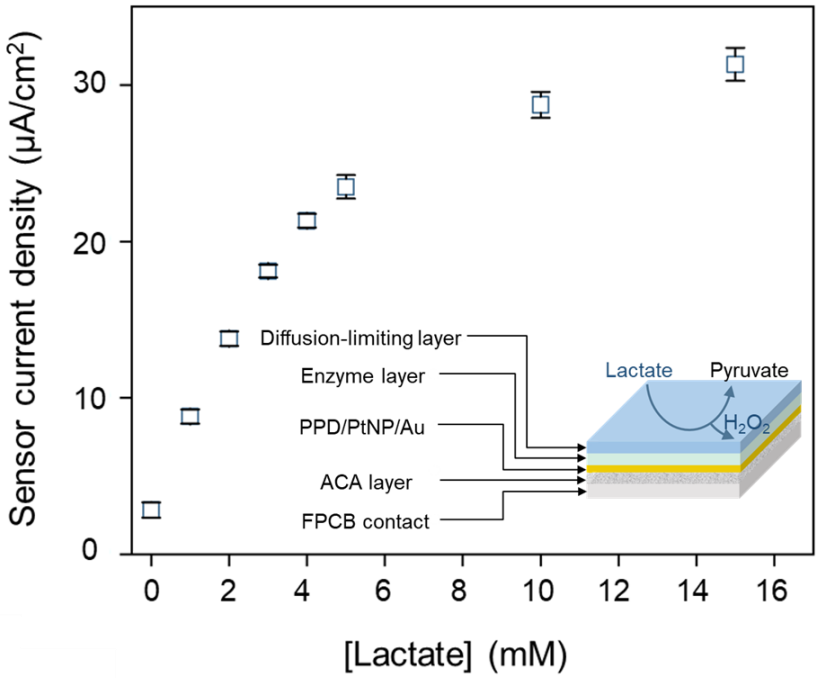

Figure 4.2: The developed lactate sensor's responses to different lactate solutions (SE, n = 3). Inset illustrates the underlying layers of the constructed lactate sensing interface.

4.2 Electrochemical sensor characterization

The developed glucose sensors were first characterized, by capturing their amperometric responses (using a standard bench-top potentiostat) to a series of solutions with different glucose concentrations (spanning the typical glucose concentration range in sweat, 0-600 μM). As shown in Fig. 4.3, the responses of the sensors to the glucose concentrations were highly linear (R^2 = 0.98). The sensors' sensitivity and the limit of detection were 15.13 ± 0.8 μA/mM/cm2 and 0.9 ± 0.05 μM, respectively.

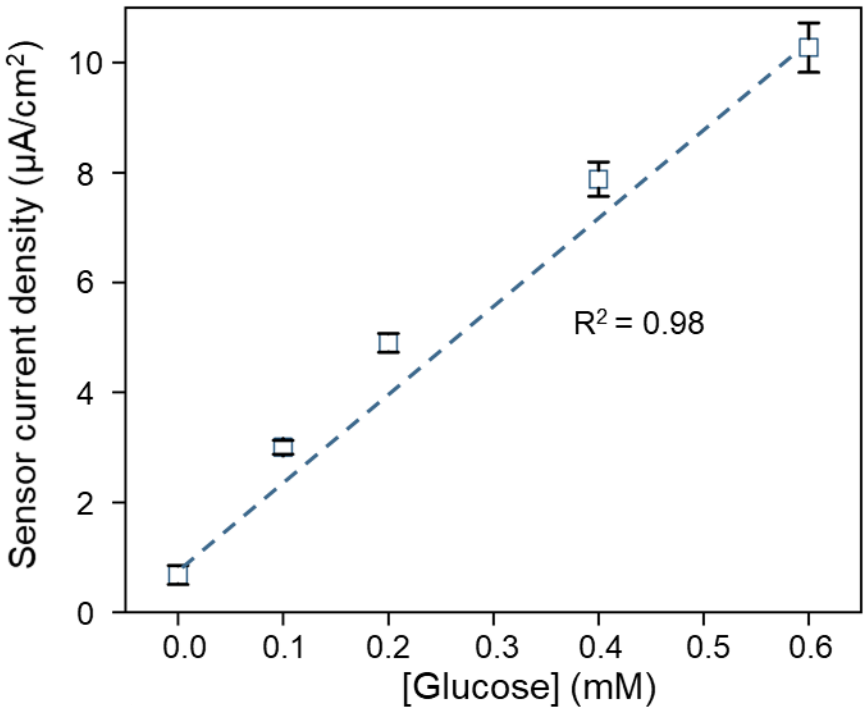

Figure 4.3: The amperometric response of developed glucose sensors (n = 3 different sensors). Error bars indicate standard error (SE).

Furthermore, the amperometric sensor responses measured by the wireless FPCB were compared with those measured by the bench-top potentiostat. The results indicated that the corresponding FPCB and bench-top potentiostat readouts were closely matched (R^2 = 0.99, Fig. 4.4), thereby validating the FPCB's reliable signal acquisition, processing, and transmission capabilities.

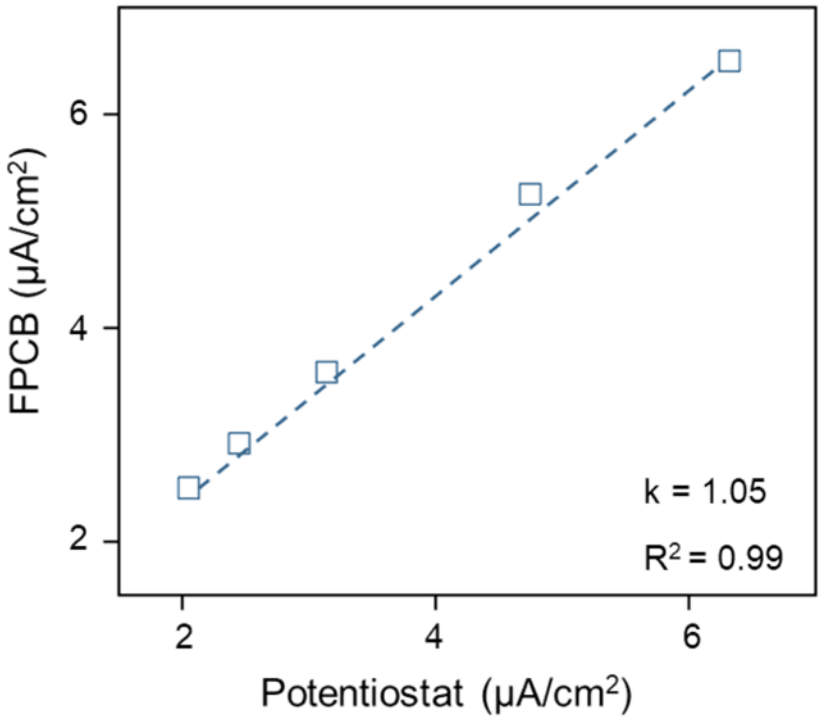

Figure 4.4: Comparison of glucose sensor readouts (current density) captured by the FPCB *vs.* potentiostat.

To ensure reliable operation in complex biomatrices such as sweat, the selectivity performance of the glucose sensor was characterized by measuring its responses to a diverse panel of physiologically relevant interfering species, including electrolytes, electroactive species, drugs, sweat agonist, proteins, and other small molecules (listed in Fig. 4.5). As shown in Fig. 4.6, the response of the glucose sensor to the interfering species was negligible, while exhibiting step-wise current responses to glucose concentration increments.

Small molecules			Ionic species		Electroactive species		Agonist	Drugs		Protein
1	2	3	4	5	6	7	8	9	10	11
Lactate	Creatinine	Choline	KCl	NaCl	UA	AA	Pilocarpine	Aspirin	Metformin	Albumin
5 mM	84 μM	1.6 μM	2.4 mM	10 mM	59 μM	10 μM	50 μM	100 μM	774 μM	1 nM

Figure 4.5: Table of common interfering molecules in sweat used for the selectivity study.

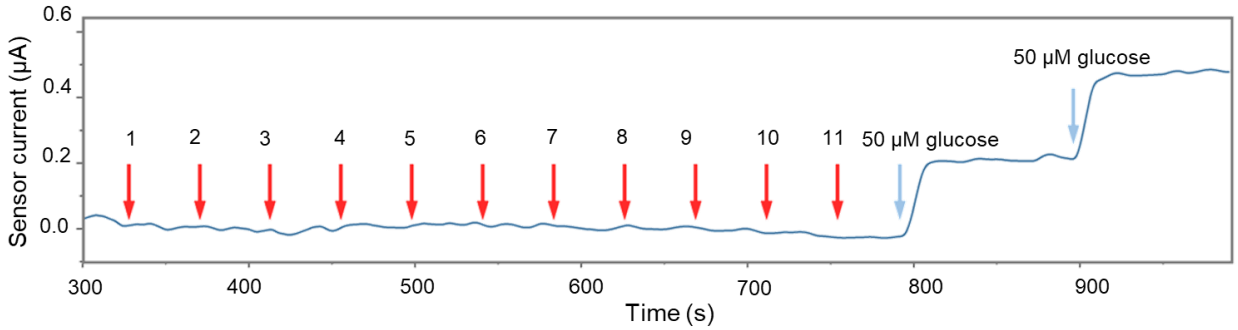

Figure 4.6: Selectivity study for the glucose sensor by monitoring its response to the sequentially-introduced interferents and glucose. The arrows indicate the introduction time points for the corresponding interferents/glucose.

To evaluate the sensors' preserved sensitivity for the duration of the envisioned on-body application (several hours), their amperometric responses were measured, in ambient conditions, every 2 hours. As illustrated in Fig. 4.7, the sensors presented minimal sensitivity variations ($\Delta <$ 4.4 %) over the period of 10-hours.

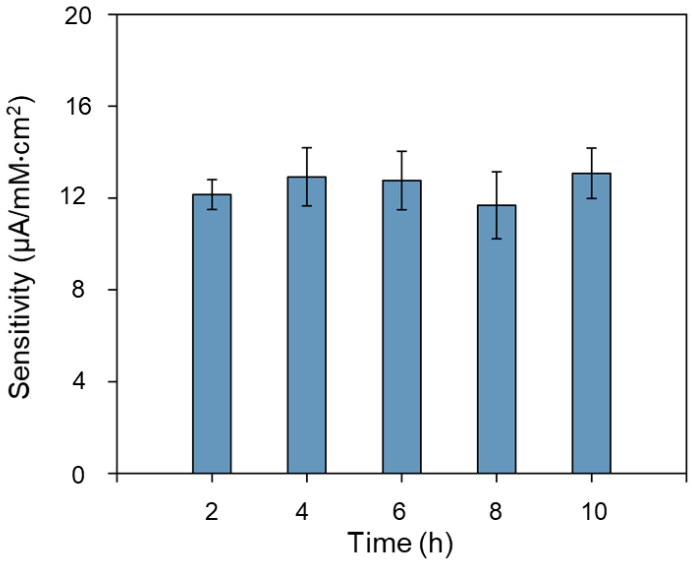

Figure 4.7: The enzymatic sensors' preserved sensitivities over 10-hour long storage at room temperature (SE, n = 3 different sensors).

Furthermore, the effect of mechanical deformation on the generated signal, along the sensor-circuit interconnection pathway (from the sensing interface to the FPCB contact pads), was characterized by recording the sensor-integrated FPCB's amperometric responses under different bending conditions (flat and α = 60°, R = 15 mm). As shown in Fig. 4.8, the induced bending had a negligible influence on the signal (< 5%).

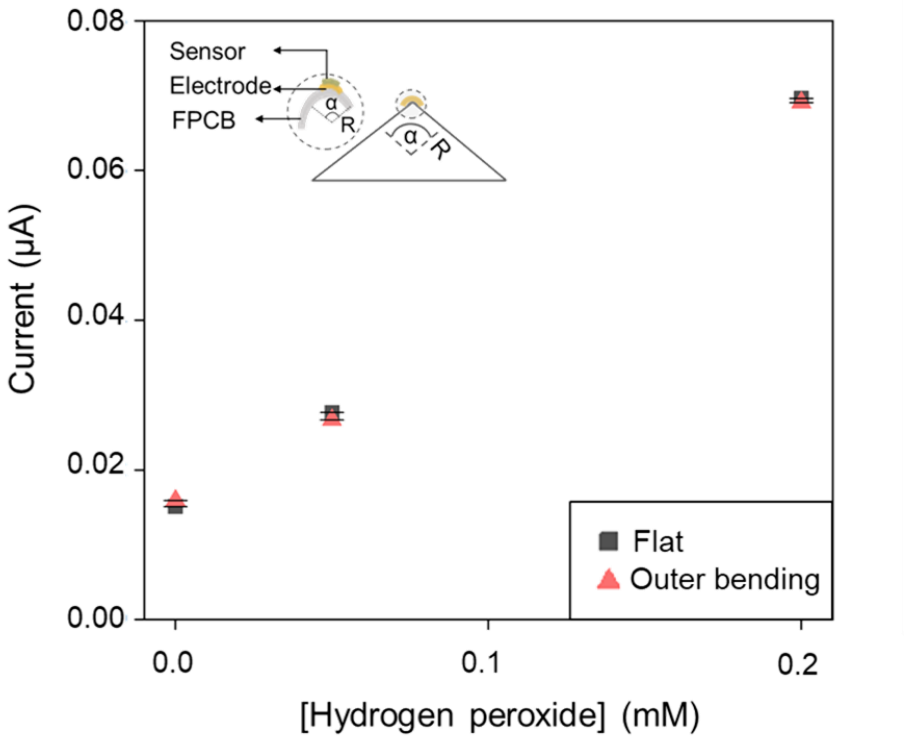

Figure 4.8: Evaluation of the PtNP/Au electrode (sensor substrate) response to hydrogen peroxide under different bending conditions (1. no bending, and 2. α = 60°, R = 15 mm).

The constancy of the adhesion between the microfluidic sensor substrate (ACA) and the circuit board's contact pad was evaluated by performing 180° peel adhesion test [27] as depicted in the inset of Fig. 4.9, and was compared to the adhesion force between the skin and the skin-adhesive layer of the microfluidic module. As shown in Fig. 4.9, the adhesion force between the skin and

the skin-adhesive layer was ~0.3 N/cm, meeting the skin adhesion limit (< 0.5 N/cm [28, 29]). The adhesion force between the microfluidic-sensing module's substrate and the circuit board metal contact pad was ~11.5 N/cm, indicating a relatively strong adhesion between the microfluidic and circuit modules (as compared to the adhesion force at the skin interface).

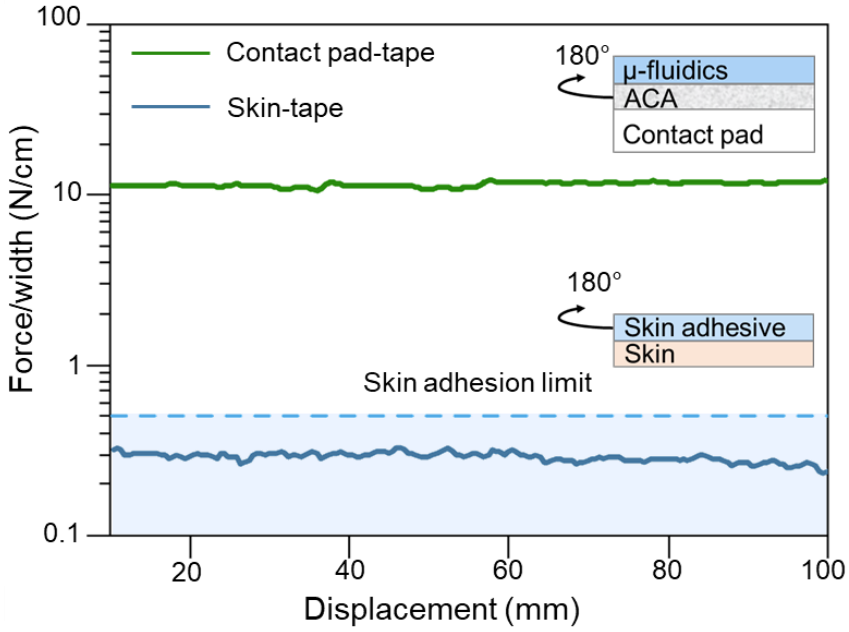

Figure 4.9: 180° peeling tests characterizing the adhesion force between the skin and tape, as well as PCB and tape. The inset demonstrates the setup of the 180° peeling test.

4.5 *Ex Situ* sweat sampling and analysis

By deploying our patch in a human subject study and following the established operational parameters, periodic sweat induction was performed at three designated time-points during a day. Upon each induction, the secreted sweat sample was directly routed and collected within the microfluidic housing in the corresponding compartment. For each case, the sweat secretion profile was optically monitored (with the aid of blue-dyes embedded in the channel). The results indicated the complete filling of the designated sweat collection chambers following a relatively consistent

secretion profile (within 30 minutes, Figs. 4.10 and 4.11). Furthermore, to illustrate the utility of periodic iontophoretic sweat sampling for constructing the diurnal profile of biomarkers, six iontophoretically-induced sweat samples were collected from a subject before/after three main meals during a day. The collected sweat samples were then analyzed using our enzymatic glucose sensors (developed following our previously reported protocol [27]). As shown in Fig. 4.12, the results indicated the elevations in sweat glucose levels upon food intake.

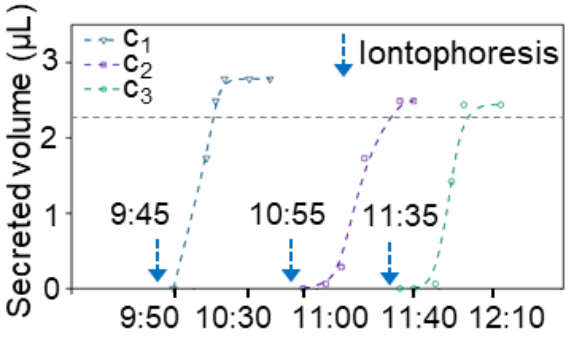

Figure 4.10: The induced sweat secretion profiles by three representative compartments in our patch at three time-points (hh:mm). Arrows mark the iontophoresis initiation (for 5 min stimulation). The dotted line marks the minimum sweat volume for biomarker analysis (© 2020 IEEE).

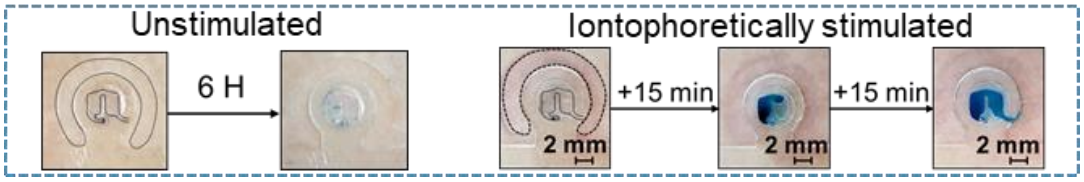

Figure 4.11: Unstimulated and iontophoretically-stimulated sweat collection into a microfluidic chamber (placed on a subject's forearm). The dotted lines depict the perimeter of the hydrogel-skin interface and the collection chamber (© 2020 IEEE).

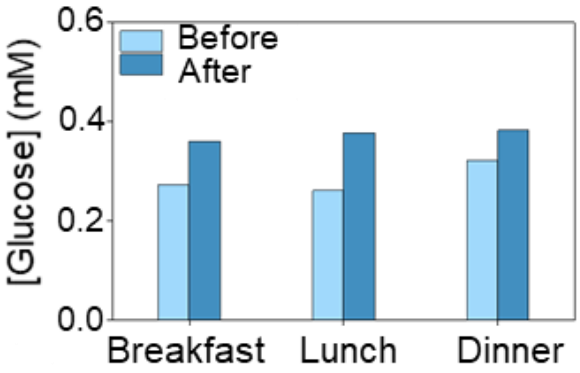

Figure 4.12: Sweat glucose levels of a subject before and after the three main meals (breakfast ~ 10:00 AM, lunch ~ 1:00 PM, dinner ~ 5:00 PM). Agonist-loaded hydrogel: 0.5% pilocarpine nitrate (PILOGEL®, reshaped to match the iontophoresis electrode footprint) (© 2020 IEEE).

Chapter 5 Integrated system for autonomous diurnal sweat sampling and analysis

5.1 Design of the hybrid-flexible FPCB module

At its core, the electronic module houses a microcontroller (MCU) unit (STM8L – UFQFN20, STMicroelectronics). The MCU was programmed to facilitate system-level functionalities (*i.e.* controlling the iontophoresis and sensing circuitries), data analysis, signal transduction through Bluetooth, and plotting the signal readouts on an onboard LCD screen (st7735 – TFT-LCD, Sitronix Technology Corporation) in real-time. A programmable current source based on a unity-gain difference amplifier (AD8276 – 8MSOP, Analog Devices) was designed to realize tunable iontophoretic actuation. This current source was integrated with an overcurrent protection circuitry using a current shunt monitor (INA282 – 8SOIC, Texas Instruments) as well as software and hardware current control mechanisms that utilize the MCU's Analog-to-Digital (ADC) and Digital-to-Analog (DAC) modules (controlled programmatically on the MCU and through the custom-developed smartphone application). With on-demand switching capabilities, the onset of iontophoresis activation at each compartment was actively controlled. A potentiostat chip (LMP91000, Texas Instruments) was programmed to generate and maintain the + 0.3 V potential across the sensing electrodes and continuously measure the amperometric output of the sensor (~ 40 minutes, after sweat stimulation before/after each meal intake). The analog-front-end in this circuit converted the measured current to voltage. To mitigate the interfering high-frequency noise, the output voltage was filtered out through a fifth-order low pass filter (MAX7422 chip – Maxim Integrated, LPF) with a cut-off frequency of 1 Hz.

5.2 Wireless FPCB module: system-level integration

The custom-developed wireless FPCB module integrates the required circuitries to implement system-level operations, including addressable and programmable iontophoretic-actuation and electrochemical sensor signal acquisition *via* six dedicated channels, as well as signal processing, and real-time biomarker data display (Fig. 5.1).

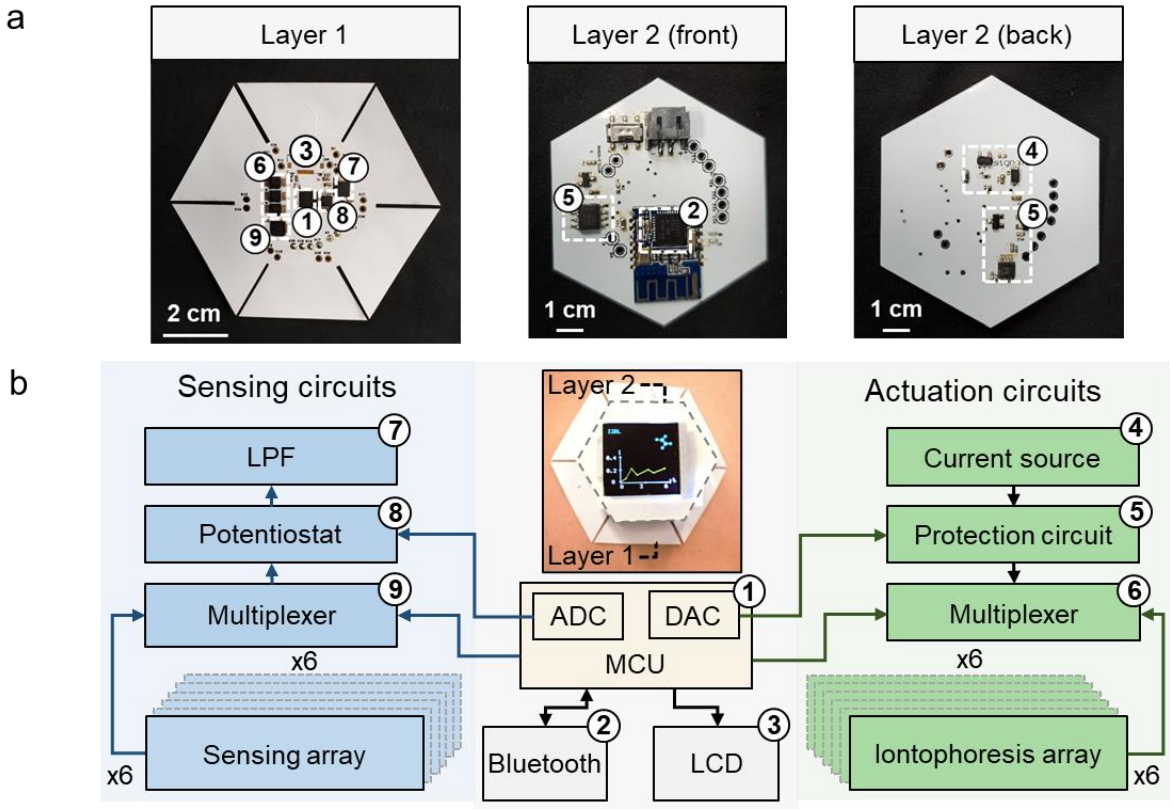

Figure 5.1: a) Optical images of the two-layered FPCB module. Layer 1 features the sensing circuitry (at the center) and iontophoretic electrode array (mechanically flexible flaps). Layer 2 features the iontophoretic circuitry and the data transmission/display interfaces. b) The system-level block diagram of the circuit operations.

This FPCB can bilaterally communicate with a custom-developed smartphone application, *via* Bluetooth, to receive/transmit the command signals (to set the desired mode of operation for each of the compartments) and the biomarker data. Upon processing the received command signals, the MCU automatically activates the iontophoretic circuitry and addresses the desired compartments (with the aid of multiplexers) to perform sweat stimulation at the intended time points (following the instructed iontophoresis settings). After the deactivation of the iontophoresis circuitry and following the MCU-generated instructions, the electrochemical sensing circuit continuously samples and processes the amperometric signal, thereby rendering biomarker data acquisition (Fig. 5.2).

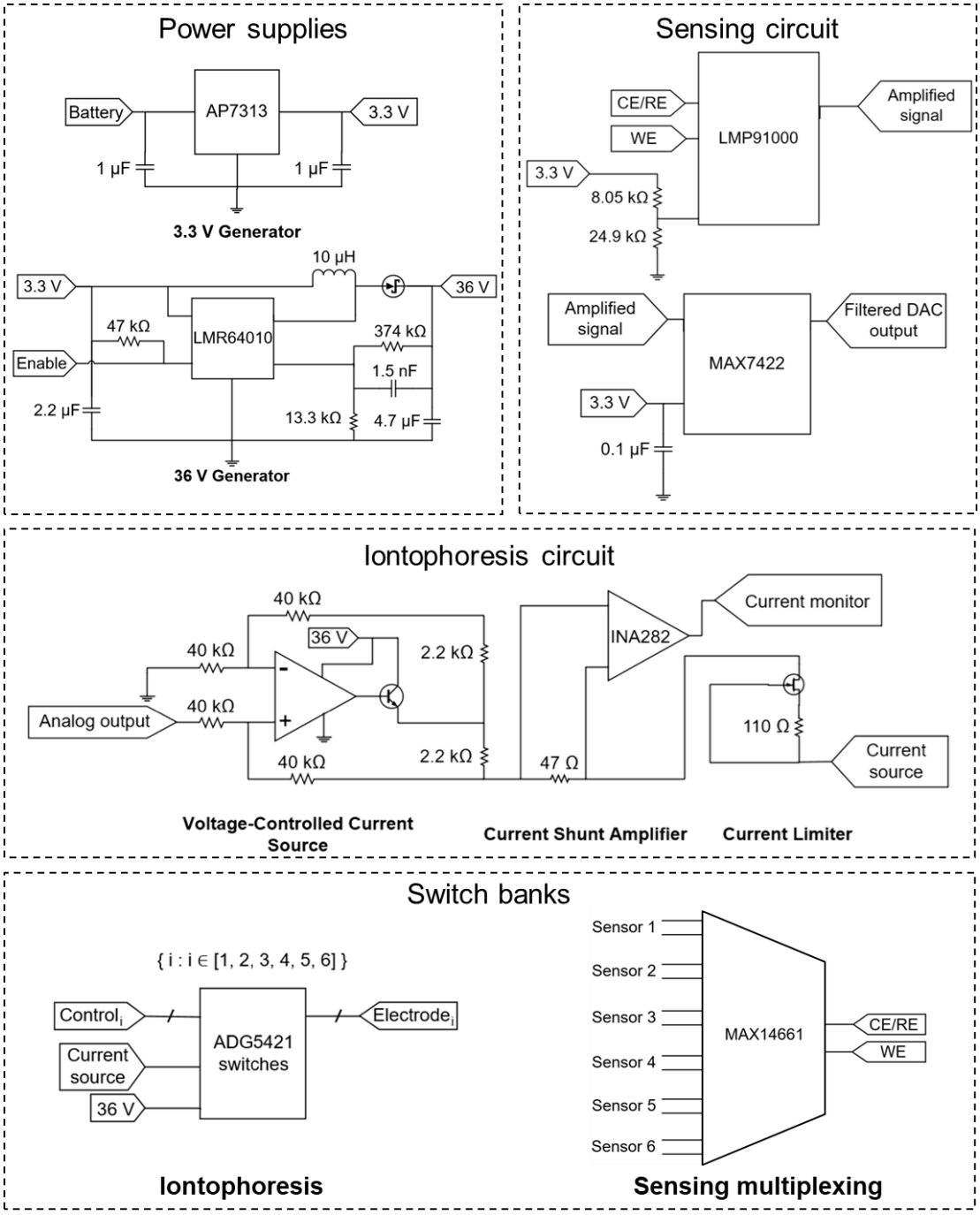

Figure 5.2: Schematic diagram of the wireless FPCB's circuitries.

5.3 Power consumption calculation

The electronic module (developed based on low/ultra-low power integrated circuit chips) is powered with a single miniaturized rechargeable lithium-ion polymer battery with a nominal

voltage of 3.7 V. The battery is embedded within a 3D-printed case, which also contains the LCD display and an FPCB module (Fig. 5.3). Based on our characterization results (without further power optimization), the core operations (*e.g.*, iontophoresis, sensing, and bilateral wireless communication) altogether demand supply current on the order of ~ 100 mA. For the demonstrated study, which includes periodic sweat sampling (5 minutes of active iontophoresis) and analysis (~ 40 minutes of sensing operation) at 6 points during the day (*i.e.*, monitoring the glucose levels before/after main meals), a battery with a capacity rating on the order of 100 mAh = (150 mA × 0.08 h + 7 mA × 0.67 h) × 6 times/day would meet the diurnal monitoring requirement. It is worth noting that if higher power levels are required, commercially available miniature lithium-ion polymer batteries with larger capacity can be used, or alternatively, the used battery can be recharged (assuming that the standard discharge requirements are met).

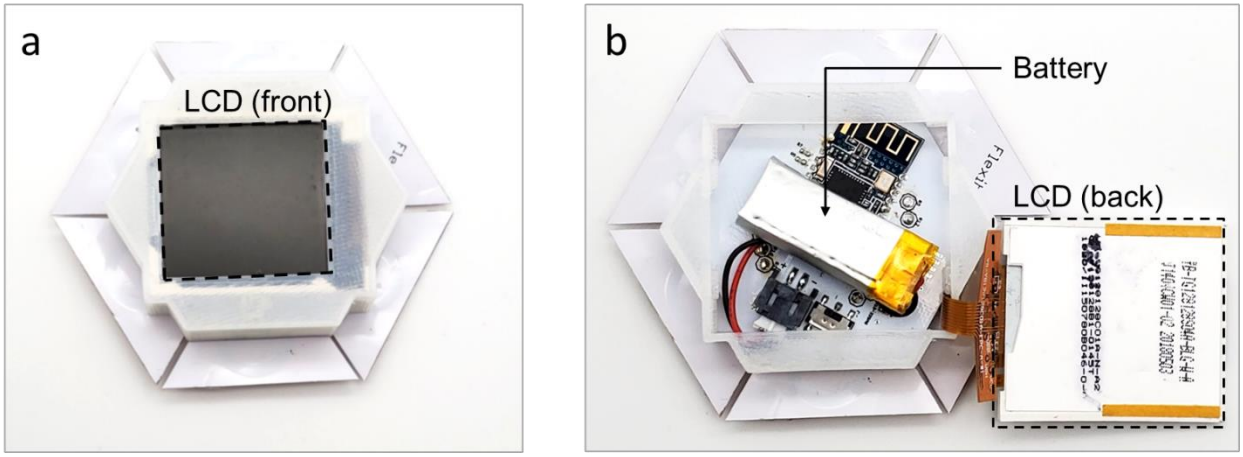

Figure 5.3: Photographs of the system illustrating the LCD display (a) and a rechargeable lithium-ion polymer battery with 150 mAh capacity (b) enclosed by/embedded within a 3D-printed case.

5.4 Human subject testing and institutional review board (IRB) approval

The conducted human subject experiments were performed in compliance with the protocols approved by the Institutional Review Board (IRB) at the University of California, Los Angeles (no. 17-000170) and the IRB at Stanford University (no. 31310). Healthy subjects were recruited based on the approved IRB protocols. All subjects gave written informed consent before participation in the study. Prior to the on-body experiments, the forearm was cleaned with isopropyl alcohol (Sigma-Aldrich), rinsed with deionized (DI) water, and wiped with Kimwipes (Kimtech Science), followed by mounting the device on the forearm. For *in-situ* sample analysis, amperometry recording began after 5 minutes of iontophoresis and following a 10-minute wait-time for the initiation of sweat secretion. The corresponding biomarker data was taken after a ~ 30-minute wait-time to ensure sufficient sweat sample accumulation (for reliable analysis).

5.5 Diurnal and programmable *in-situ* sweat sampling

The complete hybrid-flex system—consisting of the microfluidic-sensing and iontophoresis interfaces, integrated with the two-layered FPCB module—was deployed to acquire biomarker data at intermittent periods during the day and capture the biomarker's diurnal profile. Specifically, it was utilized to monitor the sweat glucose levels of a human subject over six periods—before and after the consumption of three main meals during a day—where the sweat glucose readings during each period were captured by a designated compartment. Before and after each meal intake, sweat was iontophoretically stimulated for 5 minutes at 0.6 mA, and with the aid of the inbuilt pressure of the stimulated sweat glands, the harvested sweat sample was routed to and subsequently analyzed within the microfluidic sensing chamber of the same designated compartment (Fig. 5.4a). As shown in Fig. 5.4b, the changes in the baseline of the acquired diurnal

sweat glucose profile reflected the elevation in glucose levels upon meal intake. This trend is aligned with previously reported observations, in which manual intervention was required to capture the glucose level for each time period [30].

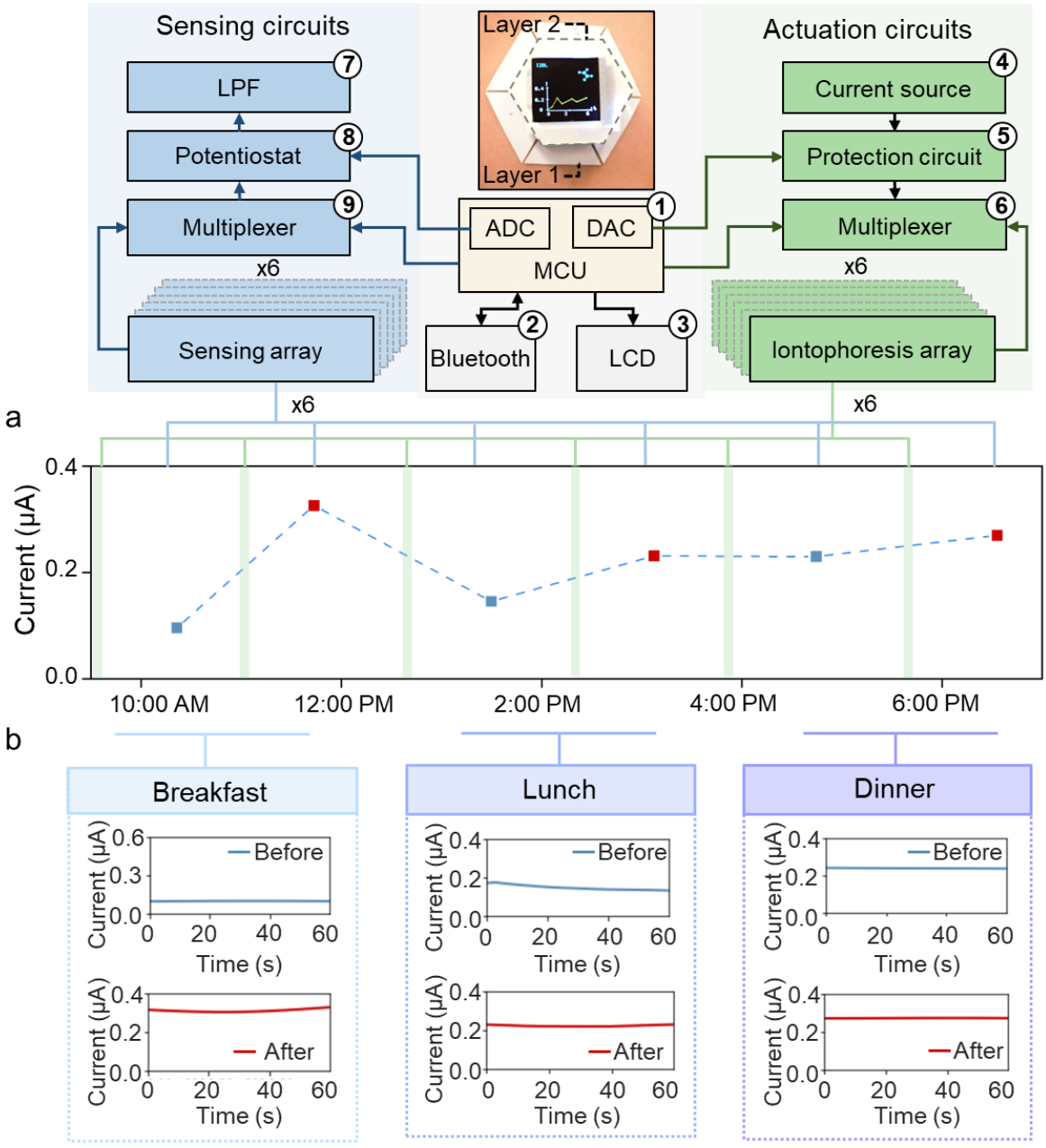

Figure 5.4: a) Diurnal sweat glucose profile (specifically, before and after main meal intakes, breakfast ~ 10:30 am, lunch ~ 2:00 pm, dinner ~ 5:30 pm), captured *via* on-body

autonomous sweat sampling and analysis (by our system). b) Representative real-time amperometric recording of glucose sensors corresponding to the diurnal sweat glucose profile shown in Fig. 5.4a.

Chapter 6 The custom-developed mobile application

6.1 Design and cloud server storage

The custom-developed Android application provides an interactive graphical user interface to wirelessly activate/deactivate the desired compartment, and independently, control the corresponding iontophoresis and sensing modalities. Additionally, this mobile application timestamps, stores, and displays the delivered iontophoresis current and the sensor readouts in real-time. This application also provides the option to synchronize and store the collected data on a Google cloud server for further analysis (Figs. 6.1 and 6.2).

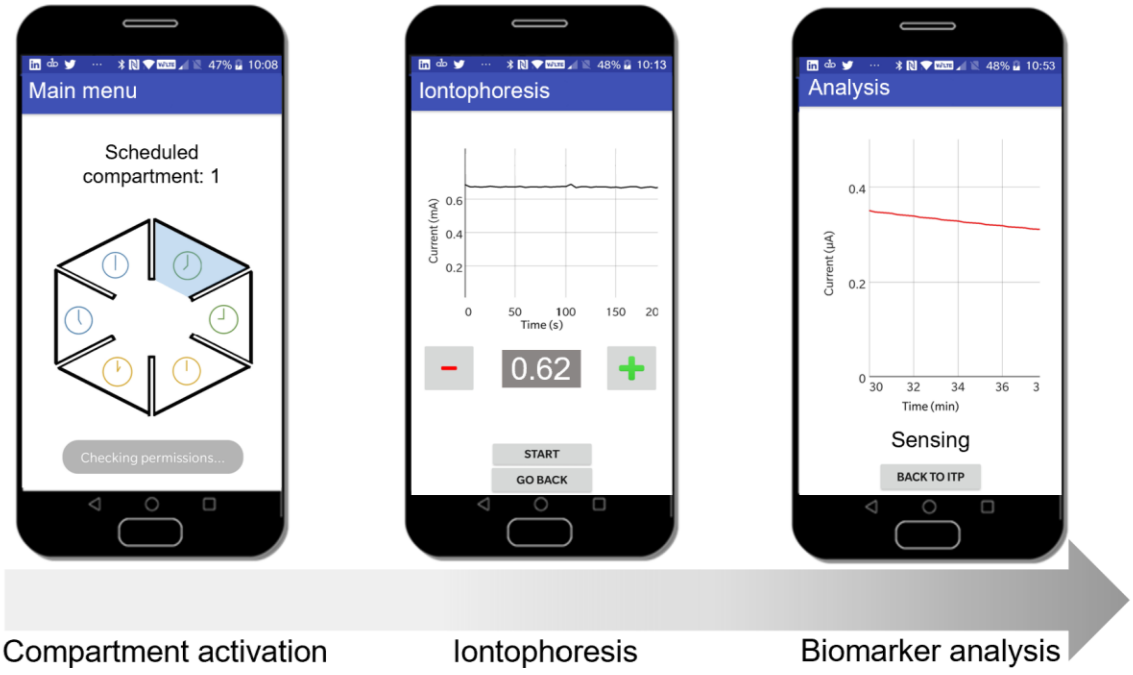

Figure 6.1: The custom-developed mobile application to control compartmentalized operations (programmable iontophoresis and sensing) and data display/storage.

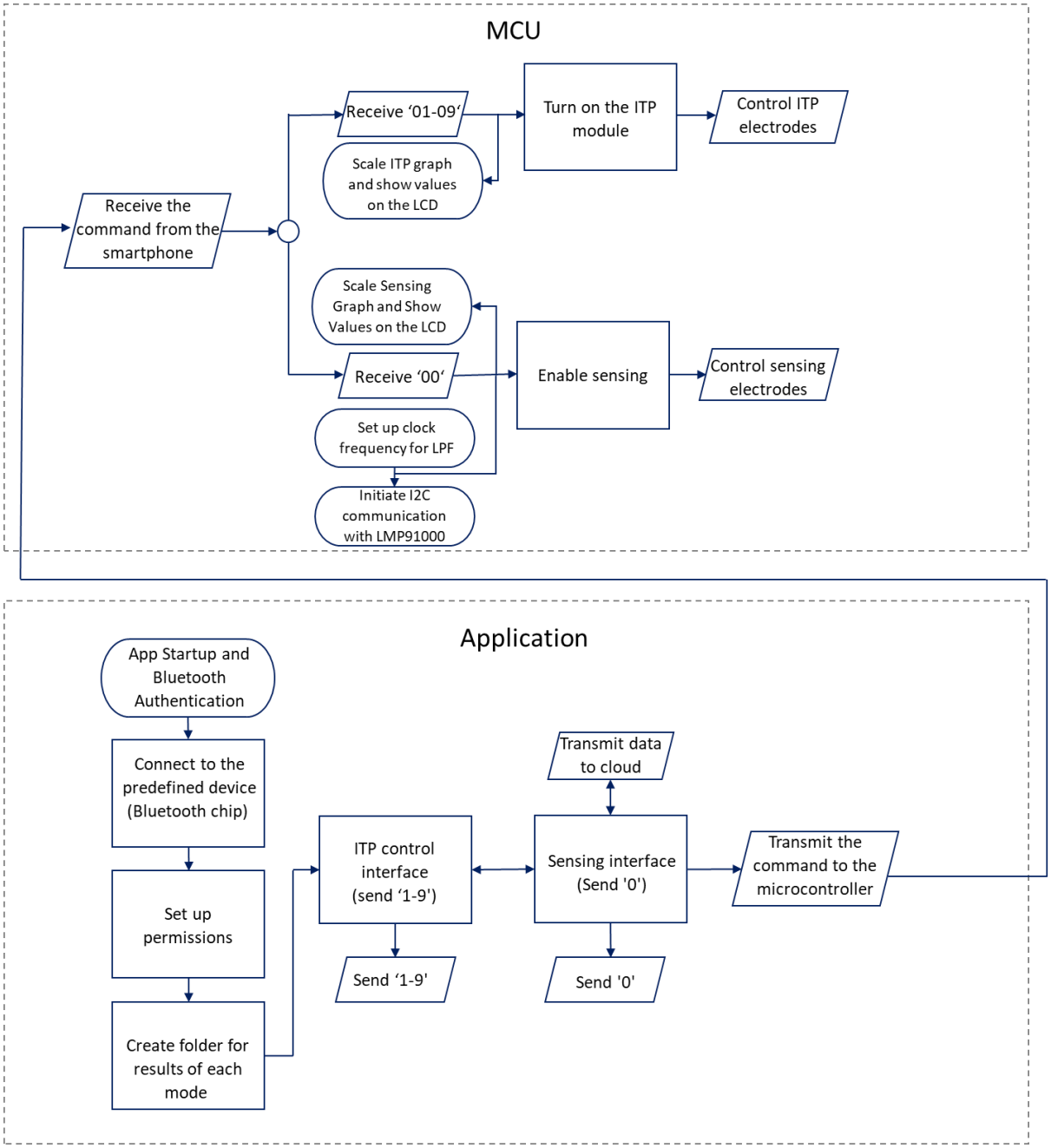

Figure 6.2: Flow chart of the communication commands and execution steps at mobile application-level and microcontroller-level for activation and control of a compartment.

Chapter 7 Discussion and outlook

7.1 Discussion

Here, we devised a hybrid-flex multi-compartment autonomous wearable system, where each compartment can be activated, at desired time periods, to induce sweat—at programmable secretion rates—for *in-situ* biomarker analysis. To inform its clinical utility, we deployed this system in a human subject study aimed at tracking the diurnal sweat glucose profile, in which the results illustrated the elevation of sweat glucose upon the intake of each of the three main meals. The autonomous functionality and multi-compartment configuration of our solution eliminate the need for manual intervention for the device substitution (unlike the previously reported solutions requiring pristine microfluidic/sensor unit replacements to avoid sample/sensor contamination). Equivalently important, the demonstrated autonomous sweat acquisition and analysis capability can be exploited to adaptively sample contextual biomarker readings based on the user's need, behavior, and activity.

Furthermore, the generalizability of the introduced sensing system design and integration methodology allows for the integration of other electrochemical sensing interfaces to track the diurnal profiles of a wide panel of biomarkers. To this end, the previously reported wearable sensor development protocols can be leveraged but may need to be optimized, to allow for sensor fabrication on an ACA substrate and vertical integration with our sensing system. Moreover, the mechanical flexibility of our device allows for its adherence to various body parts, enabling its use in clinical investigations aiming to study the correlation of sweat biomarker compositions secreted from different body sites. Additionally, the versatility of our system design allows for the incorporation of auxiliary sensing interfaces (*e.g.*, sweat pH, temperature), which could be helpful

in calibrating the sensor responses for more accurate biomarker level estimation and mitigating the confounding effects due to inter/intra-individual variations.

7.2 Outlook

Toward translating this technology into personal health monitoring applications, large-scale and longitudinal studies are required to contextualize the diurnal sweat biomarkers' data in relation to the user's nutrition (composition, timing, and frequency of meal intakes), activities, and other physiologically-relevant parameters. Augmenting data analytics techniques with the datasets harnessed by our scalable technology enables the establishment of clinical criteria to interpret sweat biomarkers' readings and provide actionable/personalized feedback to users. In this way, we can establish a non-invasive biomarker monitoring modality that can be scaled across the general population for personalized healthcare.

References

1. A. Koh, D. Kang, Y. Xue, S. Lee, R. M. Pielak, J. Kim, T. Hwang, S. Min, A. Banks, P. Bastien, M. C. Manco, L. Wang, K. R. Ammann, K. I. Jang, P. Won, S. Han, R. Ghaffari, U. Paik, M. J. Slepian, G. Balooch, Y. Huang and J. A. Rogers, *Sci. Transl. Med.*, 2016, **8**, 366ra165.

2. W. Jia, A. J. Bandodkar, G. Valdés-Ramírez, J. R. Windmiller, Z. Yang, J. Ramírez, G. Chan and J. Wang, *Anal. Chem.*, 2013, **85**, 6553–6560.

3. W. Gao, S. Emaminejad, H. Y. Y. Nyein, S. Challa, K. Chen, A. Peck, H. M. Fahad, H. Ota, H. Shiraki, D. Kiriya, D. H. Lien, G. A. Brooks, R. W. Davis and A. Javey, *Nature*, 2016, **529**, 509–514.

4. H. Lee, C. Song, Y. S. Hong, M. S. Kim, H. R. Cho, T. Kang, K. Shin, S. H. Choi, T. Hyeon and D. H. Kim, *Sci. Adv.*, 2017, **3**, e1601314.

5. S. Emaminejad, W. Gao, E. Wu, Z. A. Davies, H. Y. Y. Nyein, S. Challa, S. P. Ryan, H. M. Fahad, K. Chen, Z. Shahpar, S. Talebi, C. Milla, A. Javey and R. W. Davis, *Proc. Natl. Acad. Sci. U. S. A.*, 2017, **114**, 4625–4630.

6. W. Gao, H. Y. Y. Nyein, Z. Shahpar, H. M. Fahad, K. Chen, S. Emaminejad, Y. Gao, L. C. Tai, H. Ota, E. Wu, J. Bullock, Y. Zeng, D. H. Lien and A. Javey, *ACS Sensors*, 2016, **1**, 866–874.

7. B. Schazmann, D. Morris, C. Slater, S. Beirne, C. Fay, R. Reuveny, N. Moyna and D. Diamond, *Anal. Methods*, 2010, **2**, 342–348.

8. J. Kim, I. Jeerapan, S. Imani, T. N. Cho, A. Bandodkar, S. Cinti, P. P. Mercier and J. Wang, *ACS Sensors*, 2016, **1**, 1011–1019.

9. A. J. Bandodkar, D. Molinnus, O. Mirza, T. Guinovart, J. R. Windmiller, G. Valdés-Ramírez, F. J. Andrade, M. J. Schöning and J. Wang, *Biosens. Bioelectron.*, 2014, **54**, 603–609.

10. A. J. Bandodkar, V. W. S. Hung, W. Jia, G. Valdés-Ramírez, J. R. Windmiller, A. G. Martinez, J. Ramírez, G. Chan, K. Kerman and J. Wang, *Analyst*, 2013, **138**, 123–128.

11. W. Gao, H. Y. Y. Nyein, Z. Shahpar, H. M. Fahad, K. Chen, S. Emaminejad, Y. Gao, L. C. Tai, H. Ota, E. Wu, J. Bullock, Y. Zeng, D. H. Lien and A. Javey, *ACS Sensors*, 2016, **1**, 866–874.

12. S. Lin, B. Wang, Y. Zhao, R. Shih, X. Cheng, W. Yu, H. Hojaiji, H. Lin, C. Hoffman, D. Ly, J. Tan, Y. Chen, D. Di Carlo, C. Milla and S. Emaminejad, *ACS Sensors*, 2020, **5**, 93–102.

13. H. C. Losty, H. Wheatley and I. Doull, *Ann. Clin. Biochem.*, 2006, **43**, 375–381.

14. V. A.LeGrys, R.Applequist, D. R.Briscoe, P.Farrell, R.Hickstein, S. F.Lo, R.Passarell, D. W.Rheinheimer, B. J.Rosenstein and J. E.Vaks, Clinical and Laboratory Standards Institute, CLSI, 2009, **29**, C34-A3.

15. M. R. Prausnitz, *Adv. Drug Deliv. Rev.*, 1996.

16. T. ROSENDAL, *Acta Physiol. Scand.*, 1943, **5**, 130–151.

17. Wescor, MACRODUCT SWEAT COLLECTION SYSTEM instruction/service manual Model 3700 SYS, 2004.

18. R. M. Fish and L. A. Geddes , Eplasty, 2009, **9** , e44.

19. D. M. Sletten, K. Kimpinski, S. D. Weigand and P. A. Low, *Auton. Neurosci. Basic Clin.*, 2009, **150**, 127–130.

20. H. Lin, J. Tan, J. Zhu, S. Lin, Y. Zhao, W. Yu, H. Hojaiji, B. Wang, S. Yang, X. Cheng, Z. Wang, E. Tang, C. Yeung and S. Emaminejad, *Nat. Commun.*, 2020, 11, 4405.

21. J. Tan, H. Lin, S. Lin, W. Yu, J. Zhu, Y. Zhao, X. Cheng, S. Yang, E. Tang and S. Emaminejad, *J. Microelectromechanical Syst.*, 2020, 1–3.

22. H. Lin, Y. Zhao, S. Lin, B. Wang, C. Yeung, X. Cheng, Z. Wang, T. Cai, W. Yu, K. King, J. Tan, K. Salahi, H. Hojaiji and S. Emaminejad, *Lab Chip*, , DOI:10.1039/c9lc00418a.

23. B. Wang, B. Koo, L. W. Huang and H. G. Monbouquette, *Analyst*, 2018, **143**, 5008–5013.

24. X. Wen, B. Wang, S. Huang, T. "Leo" Liu, M. S. Lee, P. S. Chung, Y. T. Chow, I. W. Huang, H. G. Monbouquette, N. T. Maidment and P. Y. Chiou, *Biosens. Bioelectron.*, 2019, **131**, 37–45.

25. C. Boehler, T. Stieglitz and M. Asplund, *Biomaterials*, 2015, **67**, 346–353.

26. X. Cheng, B. Wang, Y. Zhao, H. Hojaiji, S. Lin, R. Shih, H. Lin, S. Tamayosa, B. Ham, P. Stout, K. Salahi, Z. Wang, C. Zhao, J. Tan and S. Emaminejad, *Adv. Funct. Mater.*, 2020, **30**, 1908507.

27. Y. Zhao, B. Wang, H. Hojaiji, Z. Wang, S. Lin, C. Yeung, H. Lin, P. Nguyen, K. Chiu, K. Salahi, X. Cheng, J. Tan, B. A. Cerrillos and S. Emaminejad, *Sci. Adv.*, 2020, **6**, eaaz0007.

28. J. Kim, Y. Hwang, S. Jeong, S. Y. Lee, Y. Choi and S. Jung, *J. Mater. Chem. C*, 2018, **6**, 2210–2215.

29. L. Liu, K. Kuffel, D. K. Scott, G. Constantinescu, H. J. Chung and J. Rieger, *Biomed. Phys. Eng. Express*, DOI:10.1088/2057-1976/aa91fb.

30. H. Lee, T. K. Choi, Y. B. Lee, H. R. Cho, R. Ghaffari, L. Wang, H. J. Choi, T. D. Chung, N. Lu, T. Hyeon, S. H. Choi and D. H. Kim, *Nat. Nanotechnol.*, 2016, **11**, 566–572.